Metal Core–Shell Nanoparticle Supercrystals: From Photoactivation of Hydrogen Evolution to Photocorrosion

Yinan Fan, Michael Walls, Caroline Salzemann, Jean-Marc Noël, Frédéric Kanoufi, Alexa Courty, Jean-françois Lemineur

Metal Core-Shell Nanoparticle Supercrystals: from Photo-Activation of Hydrogen Evolution to Photo-Corrosion

Yinan Fan,[1] Michael Walls,[2] Caroline Salzemann,[1] Jean-Marc Noël,[3] Frédéric Kanoufi,[3] A. Courty, [1] Jean-François Lemineur[3]**

Y. Fan, C. Salzemann, C. Courty

Sorbonne Université, MONARIS, CNRS-UMR 8233, 4 Place Jussieu, 75005 Paris, France.

M. Walls

Laboratoire de Physique des Solides, Université Paris-Saclay, CNRS, 91405 Orsay, France.

J.-M. Noël, F. Kanoufi, J.-F. Lemineur

Université Paris Cité, CNRS, ITODYS, F-75013 Paris, France.

E-mail:

alexa.courty@sorbonne-universite.fr

jeanfrancois.lemineur@u-paris.fr

Keywords: (Supercrystals, HER, Photo-catalysis, Optical microscopy, Nanoscale degradation)

Gas nanobubbles are directly linked to many important chemical reactions. While they can be detrimental to operational devices, they also reflect the local activity at the nanoscale. In this work, supercrystals made of highly monodisperse Ag@Pt core-shell nanoparticles were first grown onto a solid support and fully characterized by electron microscopies and X-ray scattering. Supercrystals were then used as a plasmonic photo-catalytic platform for triggering hydrogen evolution reaction. The catalytic activity is measured *operando* at the single supercrystal level by high resolution optical microscopy which allows to probe gas nanobubbles nucleation at the early stage with high temporal resolution and to quantify the amount of gas molecules trapped inside them. Finally, a correlative microscopy approach and high resolution electron energy loss spectroscopy helped to decipher the mechanisms at the origin of the local degradation of the supercrystals during catalysis, namely nanoscale erosion and corrosion.

1. Introduction

Nanoparticles (NPs) made of plasmonic materials have emerged as very promising photo-catalysts for a large number of heterogeneous chemical reactions such as H_2S decomposition[1] or CO_2 reduction.[2] These NPs strongly interact with light through the collective oscillation of conduction electrons, a phenomenon known as the Localized Surface Plasmon Resonance

(LSPR).[3] During plasmon relaxation, energetic hot carriers (electrons and holes) are generated at the NP surface and local heating is produced by energy dissipation in the metal via Joule effect.[4] Both can promote chemical transformations. Indeed, the photonic excitation of the NPs can generate a chemical potential sufficient to drive a redox reaction. As detailed by Jain *et al*., the hot carriers can be seen as reagents in a chemical reaction.[5] Therefore, plasmonic photo-catalysis and photo-thermal catalysis can be used for triggering chemical reactions,[2] enhancing the Turn Over Frequency (TOF)[6] or modifying the reaction selectivity.[7,8]

After studying model systems (i.e. well separated and monometallic plasmonic NPs), researchers are now turning their attention to more complex NP structures with heterogeneous chemical compositions with a view to tuning their physico-chemical properties. For instance, bimetallic core-shell NPs[9] are promising for plasmonic catalysis to achieve higher TOFs based on the synergistic effects between the two constituents, one being plasmonic (e.g. Ag or Au) and the other being highly catalytic (e.g. Pt or Pd) but having weaker interactions with the irradiating light. In this way, the plasmon energy can be rapidly transferred to the catalytic metal through electron-electron interactions, limiting the e/h recombination step.[10]

To counteract the low light-harvesting efficiency of single plasmonic NPs, a strategy consists in assembling them into super-structures to promote cross-talk (both chemical and physical communication) between the building blocks.[11] In order to enhance the local electromagnetic field that strongly depends on inter-NP distance, one can grow supercrystals (SCs) of NPs in a bottom-up manner to create multifunctional materials. [12,13] Recent advancements have also demonstrated the rational control of NP interfacial chemistry to tune inter-NP couplings and thereby modulate the electronic conductivity of SCs.[14] Such SCs have shown great promise, particularly for Surface Enhanced Raman Scattering (SERS)[15,16] while their potential in (photo)-catalysis has been little explored. The aim of the present work is to investigate this subject by constructing and evaluating the potential of SCs composed of plasmonic and catalytically active NPs for photocatalytic chemical transformation, particularly in the context of the water splitting reaction.

In this work, SCs of Ag@Pt core-shell NPs were first synthetized and fully characterized. Then their performance for the photocatalytic hydrogen evolution (HER) reaction was evaluated. The Ag core was chosen for its highly efficient plasmonic light-harvesting properties, while the Pt shell will confer both corrosion resistance and catalytic properties, as it is the best catalytic material for HER.[17]

The extent of the photocatalytic reaction has been thoroughly scrutinized concerning both its impact on the SC structure and the products formed in the solution phase. The product formation

is monitored *operando* and in real time, at the single SC level, by high resolution label-free optical microscopy.[18] The strategy uses the production of gas as a proxy of the local catalytic activity of SCs, thanks to the large variation of refractive index between gas and water. Hence refractive-index based optical microscopies allows monitoring the evolution of gas, as molecular dissolved species or individual gas nanobubbles, at single nanoobjects.[19–24] In addition, the structural changes in the SCs associated with the photocatalytic reaction are probed through a multiscale imaging strategy. First, sub-microscale analysis is provided by a correlative (identical location) optical and scanning electron microscopy (SEM) approach.[25] Then shape and chemical nanoscale analysis (with sub-NP resolution) is obtained by Scanning Transmission Electron Microscopy using a High-Angle Annular Dark-Field detector (STEM-HAADF) analysis coupled with Electron Energy Loss Spectroscopy (EELS) elemental maps.

2. Results and discussion

2.1. NP synthesis

The Ag and Ag@Pt NPs with 1-2 Pt atomic layers were synthesized according to a previously published protocol.[26] Briefly, spherical Ag NPs of controlled size were synthesized by a high-temperature process in which $AgNO_3$ in the presence of oleylamine transforms to Ag(0) NPs whose sizes are controlled by the reaction time, heating ramp and temperature. Here, the temperature was fixed at 240°C, the heating ramp at 450°C/h and the reaction time at 1h. Next, Ag@Pt NPs were synthesized via a seed-mediated growth process in which the Ag NPs are used as seeds in presence of a Pt precursor ($Pt(acac)_2$). The Pt shell thickness is controlled by adjusting the concentration ratio between the Pt precursor and the silver seed. An optimum Pt thickness between 1-2 layers was selected. TEM images of the resulting Ag NPs and Ag@Pt NPs are presented in Figure 1a and 1b, respectively. Both types of NPs show spherical shapes with sizes of 12.7 nm and 13.4 nm for Ag and Ag@Pt NPs. The shell thickness grown on the silver core is thus around ~ 0.35 nm. The size dispersion graphs reported in Figure 1c evidence a size poly-dispersity equal to 9 % for the two colloidal systems, which is narrow enough for 3D organization,[27] thereby enabling the formation of NP SCs, see below.

The Ag core, possessing a high extinction cross section as well as a low imaginary dielectric constant in the visible, can strongly interact with light through electron-photon interaction. As a result, the extinction spectrum of the NP core (i.e. before Pt deposition) shows an intense plasmonic band centred at 403 nm, as noted in Figure 1d (blue curve). In the presence of the Pt

shell, a material with a larger imaginary dielectric constant, a significant damping of the plasmon band is measured (Figure 1d, red curves), even though the shell is ultrathin. Nevertheless, considerable light-matter coupling persists and energy can be transferred via electron-electron interactions from the Ag plasmonic core to the Pt shell. The dotted lines correspond to the theoretical extinction spectra for NPs of equivalent size and composition obtained by Mie theory. The excellent agreement found shows that the damping of the electromagnetic field enhancement upon introduction of 1-2 monolayer of atoms can be understood by Mie theory, which can thus assume a predictive role for other materials synthesis. The idea is that the e^- generated during the light excitation process should be harvested via the electrocatalytic Pt shell to drive the reduction of protons into molecular H_2. This hypothesis was verified by irradiating colloidal solutions of both Ag and Ag@Pt NPs in the presence of acid for a few minutes using a tungsten-halogen white light source. While no change is observed in the Ag NPs, a significant amount of gas is produced in presence of the bimetallic NPs (see section SI1 in supporting information, SI). This illustrates qualitatively the synergistic effect of the core-shell structure. Similar results have been published previously for the reduction of para-nitrophenol.[26]

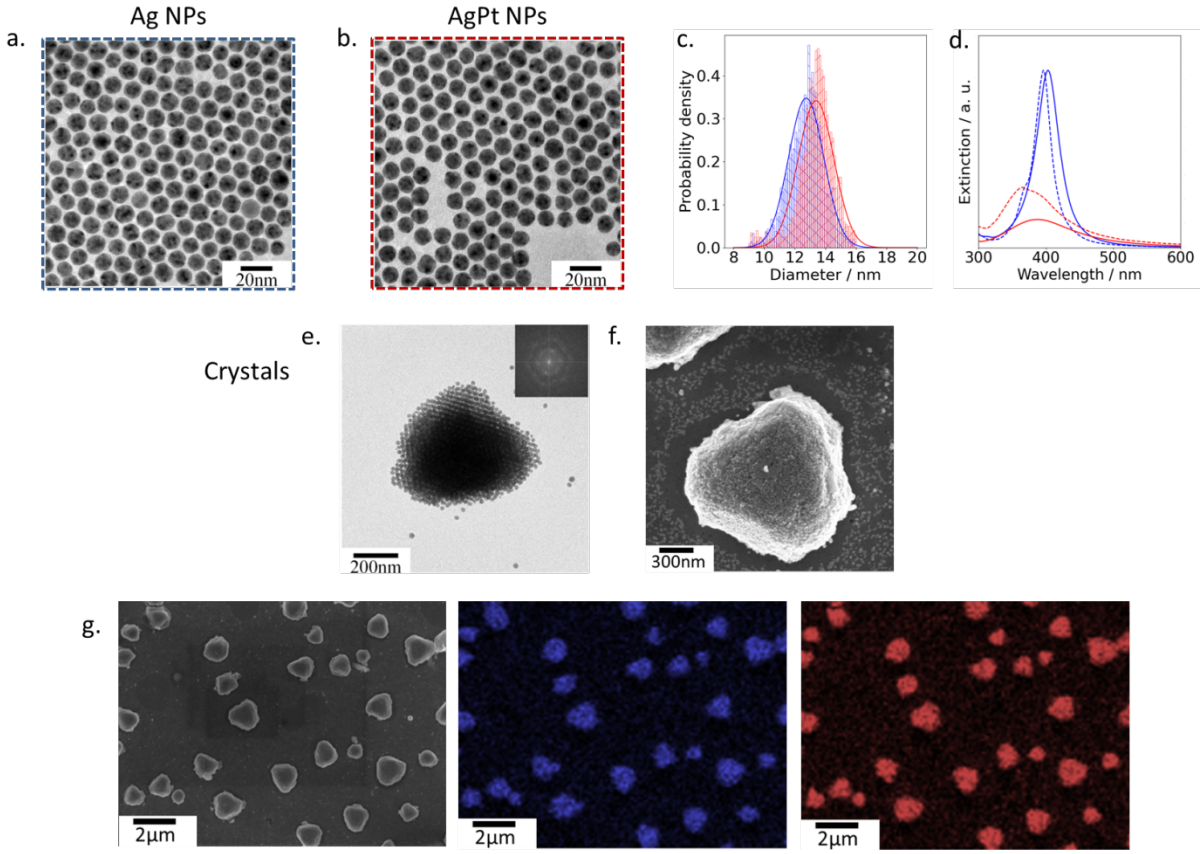

Figure 1. Step-by-step formation of colloidal super-crystals from the self-assembly of core-shell Ag@Pt NPs. TEM images (a) and (b) correspond to silver seeds and Ag@Pt NPs,

respectively. (c) Corresponding NP size dispersion graphs and (d) UV-Vis spectra of Ag and Ag@Pt NPs dispersed in toluene (experiments and Mie predictions in solid and dotted lines, respectively). Data related to silver seeds appear in blue while those corresponding to core-shell architecture are presented in red. (e) TEM and (f) SEM-FEG images of single crystals of Ag@Pt NPs obtained by drop-casting 5 µl of the corresponding colloidal solution. (g) SEM images and corresponding Ag (blue) and Pt (red) elemental EDX mapping of crystals grown on an ITO substrate.

2.2. Self-assembly into SCs

In order to develop a supported nano-catalysts platform enabling the photo-activation of HER, which could produce H_2 at high mass transfer, for instance in fluidic systems, different chemical engineering solutions have been proposed (fluidized particle beds, etc.).[28] Here, we wish to take advantage of the ability of the NPs to assemble into dense and mechanically stable SCs. This furnishes several advantages: (i) the SCs can be assembled or disassembled upon chemical stimuli (herein wetting or solvent evaporation), (ii) the NPs assemble into sub-micron to micron-sized crystals which can be easily immobilized on surfaces, (iii) the assembly further provides a higher cross-section for light absorption (leading to enhanced chemical transformation).

Ag@Pt NPs initially synthesized in oleylamine were then transferred to toluene to induce their 3D self-assembly. Toluene allows SCs to grow homogeneously by promoting Van der Waals interactions between the NPs.[29] Ag@Pt NPs, coated with oleylamine and dispersed in toluene were deposited by drop-casting 20 µL of a 0.1 mM solution of Ag@Pt NPs onto flat substrates in an inert atmosphere. The deposition is first performed on a TEM grid, using anti-capillary tweezers, in order to visualize the SCs. An image of the resulting SCs is presented in Figure 1e. The Ag@Pt NPs spontaneously self-assemble into individual quasi-triangles after the evaporation of the solvent. The inset in the TEM image of Figure 1e shows the FFT image of the individual SC, that displays well-defined spots characteristic of well-organized NPs and is typical of an *fcc* arrangement.[30]

Similarly, the depositing of the colloidal solution onto the surface of an ITO-coated glass cover-slip yields the self-assembly of the Ag@Pt NPs into individual SCs with sizes of approximately 1 µm, as observed in the SEM images of Figure 1f and 1g. The deposit was also analysed by EDX and confirmed the elemental composition of the SCs (see SI, FigureS2.1) agreeing nicely with that deduced from TEM image analysis. EDX mapping (Figure 1g, blue and red for Ag

and Pt, respectively) also shows a perfectly homogeneous repartition of Ag and Pt in the 3D structures, confirming the uniform composition of the building blocks. Indeed, in a previous article we gave evidence that the core-shell structure is homogeneous in composition.[26] No segregation has been observed. The atomic composition of Ag@Pt NPs deduced from EDX analysis agrees with the one calculated from TEM images (see Table S2.1 in SI).

Finally, the crystalline structure of the formed SCs was investigated by Grazing Incidence Small Angle X-ray Scattering (GISAXS), detailed in SI, section SI2. The GISAXS pattern confirms that the NPs are well-ordered in 3D. The diffraction spots of the GISAXS pattern can be associated with an *fcc* lattice. The clear equatorial reinforcement of the (111) and (222) diffraction lines also suggests that a large proportion of SCs present the (111) face parallel to the substrate. This is consistent with the SEM images (Figure 1f and 1g) that show a large number of triangles lying on their larger faces. One can also point out the presence of elongated spots that reflect the presence of out-of-plane stacking faults. From the positions of the Bragg reflections, the NP-NP separation distance is estimated as 3.6 ± 0.4 nm, in agreement with the presence of oleylamine, a capping ligand carrying a long alkyl chain (length 2.04 nm) and with low chain inter-digitation.

2.3. Material reactivity

2.3.1. Optical monitoring of gas NB formation

The plasmonic photo-catalytic activity of the supported SCs was scrutinized in real time using high resolution optical microscopy. As shown in Figure 2, the SCs are illuminated from the backside of the transparent ITO substrate through a high numerical aperture (NA = 1.4, oil immersion) objective. The light is then reflected by the substrate surface (red arrows in Figure 2a) and scattered by any object present at the ITO surface, for instance the SC (blue lines in Figure 2a) and further collected through the same objective by a digital camera acquiring images at 20 Hz. These particular illumination and imaging conditions, named interference reflection or interference scattering, boost the microscope sensitivity, since the optical signal collected on each pixel, I(x,y), is mainly due to the interference between the reflected and backscattered fields.[31,32] Such sensitivity is particularly useful for probing subtle local changes in refractive index associated to nanoscale chemical transformations.[19,33–35]

The light source of the optical microscope can also be used to trigger photochemical processes.[24] In this work, it appears that the white light LED source (surface power density <

5 W/cm^2) is sufficient to trigger the photo-activation of the cathodic semi-reaction corresponding to Equation 1 at the SC surface thereby enabling the evolution of H_2 gas, possibly at sufficient levels (above saturation) for the formation of H_2 gas NBs.

$2H^+ + 2e^- \rightarrow H_2$ (1)

The experimental methodology then consists in monitoring dynamically, the formation (nucleation or appearance) of gas NBs, from their early stages to their detachment from a single SC of Ag@Pt NP immobilized on a transparent ITO coated glass coverslip. The conducting ITO layer coating facilitates SEM imaging, thereby enabling identical location correlative imaging of the SC structure and distribution (see co-located SEM and optical images in Figure S4.1).

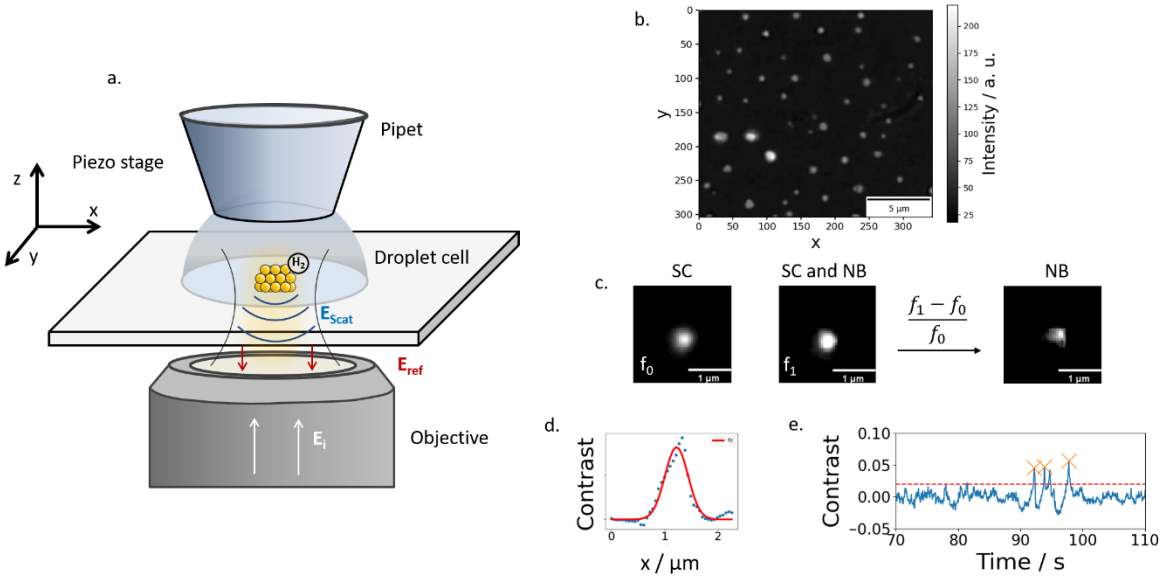

Figure 2. *Operando* optical imaging by interference reflection microscopy of NBs appearance over the super-crystals supported ITO-substrate. (a) Schematic representation of the microscopy configuration used to probe H_2 NBs produced by photoreduction of a 5 mM H_2SO_4 aqueous solution at single SCs of Ag@Pt NPs. (b) Optical image recorded in a region of interest on the ITO support. (c) Optical image before (f_0) and after (f_1) the growth of a single NB on a catalytic crystal. The optical image in (c) labeled as NB corresponds to a contrast image, representing $(f_1\text{-}f_0)/f_0$. (d) Gaussian fitting of a line profile of the resulting feature revealed in the contrast image (NB). (e) Optical intensity profile evidencing the transient generation of 3 NBs (orange crosses) at the same single crystal.

The HER at these single immobilized crystal catalysts is then actuated and dynamically probed upon contact with a 5 mM H_2SO_4 aqueous solution. In particular, the HER reaction is performed within a ca. 10^3 µm^2 area of the surface, defined by a meniscus cell confined between

a micro-pipet filled with the aqueous solution and the crystal-coated ITO substrate (see Figure 2a). This confinement technique, adapted from the scanning electrochemical cell microscope (SECCM),[36,37] allows us to target optically multiple regions of interest (ROI) on the same substrate.[38,39] Note that a rather low H^+ concentration (10 mM) has been used to avoid damaging the ITO surface that has been shown to be unstable in too acidic conditions.[20]

Figure 2b presents a typical wide field (16.5 x 21 μm^2) optical image of the crystal-coated ITO substrate contacted with the meniscus of solution. It shows 44 crystals, appearing as bright contrasted features, with sizes often larger than the diffraction limit. Images are taken successively at a frequency of 20 Hz, over several seconds, from which the dynamics of H_2 NB production can be evaluated. The strong scattering from the crystals hampers the direct visualization of single NBs (compare the Crystal, f_0, and Crystal+NB, f_1, images in Figure 2c). However, by image reconstruction, one can obtain a differential contrast image revealing, in Figure 2c (image named NB), the presence of an NB captured on the edge of the crystal. Indeed, the overall optical intensity slightly increases when an NB is nucleating on the crystal (image labeled as f_1) in comparison with the intensity related to the same crystal without an NB (image labeled as f_0). The point spread function (PSF) observed in the image f_1 of Figure 2c is then a combination of the contribution of both the crystal and the NB. Zhou *et al.* already addressed this issue to monitor the decomposition of formic acid at PdAg nanoplates.[23] They proposed to separate the two contributions (material and NB) by image subtraction to retrieve the NB PSF (see Figure 2C) that can be further used to super-localize its center of mass and therefore its anchoring site within ± 10 nm spatial resolution. From a previous optical simulation of light scattering by NBs,[19] it has been shown that when NBs appear as bright contrast features, they already have rather large diameters, i.e. more than 380 nm. This suggests that NBs can be directly sized by fitting their PSF with a Gaussian function and measuring its full width at half maximum (FWHM), taking into account that the microscope, with a NA objective of 1.4 and a mean detection wavelength λ = 510 nm possesses a PSF $\approx 1.22\lambda/NA \approx$ 220 nm. The example presented in Figure 2 suggests that a NB with diameter < 500 nm was formed by the crystal, based on the Gaussian fit shown in Figure 2d.

2.3.2. Quantification of H_2 gas production

To describe the dynamics of NB production at the same individual crystal (Figure 2c), the optical signature arising from NBs was visualized dynamically by using a slightly different image reconstruction procedure named differential rolling average method.[40] Briefly, it

consists in comparing the image frames (*f*) by dividing two consecutive stacks of (N=5) frames and to roll the operation over the whole image sequence. Then, for each pixel (x,y) in the frame f_S taken at time (S) within the image sequence, a contrast C_S is obtained following Equation 2.

$$C_S = \frac{1/N \sum_{S+1}^{S+N+1} f_i}{1/N \sum_{S-N}^{S} f} - 1 \qquad (2)$$

This image reconstruction process removes static features in the images (i.e. the SCs) and increases the signal to noise ratio (SNR) in order to distinguish single NB signals from the background intensity.

The production of NBs can then be dynamically probed during the substrate illumination. The dynamics of an NB is visualized through the evolution of local contrast with time (optical transient) extracted from a small region of interest (ROI). Such an optical transient recorded in a single crystal region is shown in Figure 2e. The events of NB formation or disappearance in this single crystal region are detected instantaneously as contrast C spikes, the formation being associated with rise in C_S, particularly above a given threshold value (displayed in red in Figure 2e), typically >2% above the noise level (ca. 0.5%). Similarly, the NB detachment from the crystal surface is associated with a fall in C_S (going back to the baseline $C_S \approx 0$).

Figure 3 summarizes 6.5 seconds of NB tracking over a rather large support surface (area ≈ 350 µm², Figure 3a) including 44 SCs. Data over a longer period of time are available in SI, section SI5. The positions of all the NBs detected during the optical monitoring are represented by the red dots in Figure 3a. It can be noted that all the NBs seem to grow onto or close to single crystals and therefore act as reporters of the local catalytic activity of individual SCs. Based on the NBs coordinates, less than ~40 % of SCs are active during this time lapse. In addition, counting the number of NBs formed over the experiment yields the rate of NB production events. As attested by the NB counting and the linear evolution of the cumulative count shown in Figure 3b, the rate of NB production is constant over time and is evaluated to ~ $2\ 10^{-2}$ NBs $\mu m^{-2} s^{-1}$. However, the rate is not constant everywhere on the support, as detailed in SI5.2, and mostly depends on the structural characteristics (shape or NPs stacking faults for instance) of the drop-casted SCs and their surface density.

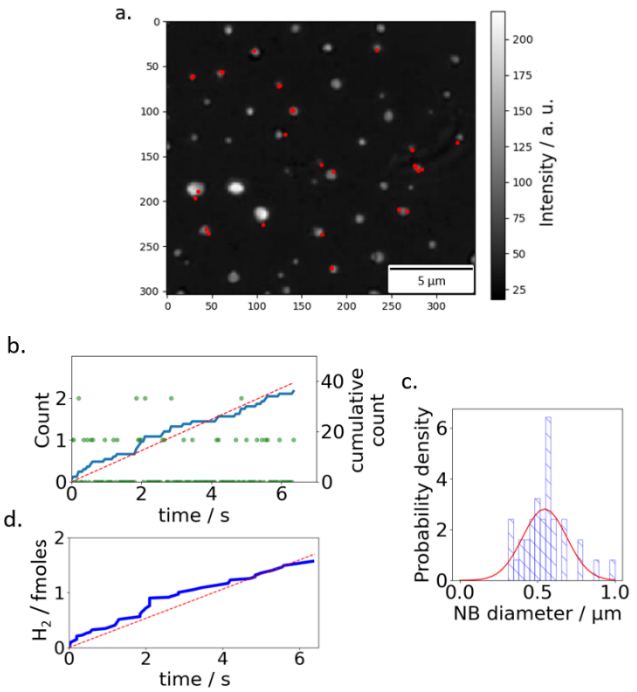

Figure 3. Mapping and quantification of H_2 production at SCs supported on a solid substrate. (a) Optical mapping of NB nucleation events over 44 SCs during 6.5 seconds of white light irradiation. The super-localization of the nucleation events are represented by red dots. (b) NB counting over time in the region imaged in (a). (c) Size dispersion graph for gas NBs obtained by systematic fitting of each NB PSF as shown in Figure 2d. (d) H_2 gas production calculated from (b) and (c).

Next, we analysed the stochastic appearance and detachment of NBs to evaluate the amount of H_2 associated with NB production over the imaged region. The PSF of every probed NB, just before they detached, was fitted by a Gaussian function to extract its FWHM. An example of such a PSF and corresponding fit is shown in Figure 2d. Here, the FWHM is used as a proxy of the final NB size and to calculate the final NB volume, V_{NB}, following Equation 3 assuming the NBs detach as spheres from the nanostructured SC.

$$V_{NB} \approx \frac{4}{3}\pi\left(\frac{FWHM}{2}\right)^3 \qquad (3)$$

The amount of H_2 gas contained inside the NB, n_{H_2}, can further be estimated from V_{NB} and Equation 4 assuming the ideal gas situation.

$$n_{H_2} = \frac{V_{NB}P_L}{k_B T} \qquad (4)$$

where k_B is the Boltzmann constant and T the temperature. The internal pressure (P_L) for spherical NBs is calculated using the Young-Laplace equation:

$$P_L = P_0 + \frac{4\gamma}{r} \qquad (5)$$

where P_0 is the ambient pressure (1 atm), γ the aqueous solution surface tension (72.8 mN/m) and r the NB radius (r ≈ FWHM/2). Typically, a 0.5 µm NB would hold a 12 atm Laplace pressure, carrying 2 10^7 molecules or 0.035 fmoles of H_2 gas.

From the NB size dispersion graph presented in Figure 3c one can reconstruct the evolution of n_{H_2} over time presented in Figure 3d. As the NBs have rather similar sizes (0.5 µm in average) and as the NB nucleation frequency is constant over time, H_2 production also appears constant over time. From the 1.6 fmoles of H_2 gas detected during the 6.5 s experiment presented in Figure 3d, the production rate of H_2 molecules rises to ~ 4.5 10^5 mol.µm^{-2} s^{-1}. Considering that the crystals occupy a fraction $\rho \sim 7$ % of the area in the ROI, the equivalent photocurrent j resulting from proton reduction amounts to $j = 2 \times rate \times q_e/\rho \sim 0.2$ mA/cm² of active surface, with $q_e = 1.6\ 10^{-19}$ C, the elementary charge of the electron.

2.3.3. Plasmonic photo-catalysis at single SCs

We then turned our attention to the production of molecular hydrogen by individual SCs. Figure 4 summarizes the three distinct behaviours in photo-catalytic activity observed at the single SC level. From the typical contrast intensity transients in Figure 4a: (i) some SCs show a rather constant activity, giving a production rate of ~ 0.2 NB per second, that does not fluctuate much over time; while other crystals (ii) exhibit intermittent activity or (iii) appear not to be active at all in the course of the experiment. In the latter case (54 % of the SCs in the ROI in Figure 3a) the intensity transients in the SC region do not show any spikes.

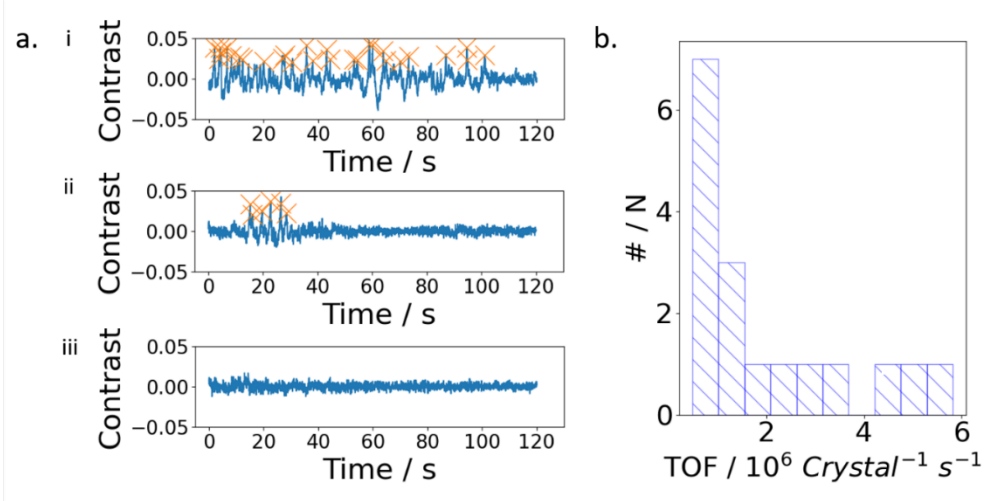

Figure 4. Hydrogen production at the single SC level. (a) Optical intensity transients in three single SC regions summarizing three distinct behaviours: (i) constant photo-catalytic activity, (ii) intermittent H_2 NB production and (iii) absence of photo-activity. (c) Distribution of turn-over frequency at single crystals.

As previously stated, the occurrence of a spike in the optical transient reveals the formation and subsequent detachment of a single NB whose size is inferred from its FWHM. It is used similarly to calculate from the contrast time trajectory in Figure 4a (i) the total number of H_2 molecules generated by the single SC over time. This production rate per SC is analogous to the turn-over frequency (TOF) for an individual SC, which can be further determined for all the imaged crystals, as reported in Figure 4c. The distribution of the TOFs for the probed active SCs is in the range of around 10^6 H_2 mol.SC^{-1}.s^{-1} or equivalently 0.3 pA.SC^{-1}. In comparison, for an ultramicroelectrode (UME) of similar size (1 μm in diameter), the mass-transfer-limited reduction of protons would amount to ~ 2 nA, which is about 10^4 times higher than the equivalent photocurrent supported by a SC.

2.3.4. Reaction mechanism and degradation

SC erosion

Many studies have reported that structured substrates frequently reorganize during gas evolution [41] and that the catalysts often undergo reaction induced chemical degradation. Such effects should be problematic in photocatalytic systems where an e^-/h^+ pair is produced, since the e- is harvested for HER, the h+ may have a deleterious effect if not carefully harvested into another useful reaction. This is not usually a problem, as photocatalytic reactions normally employ a sacrificial donor to evacuate the photogenerated h^+. Here the aqueous solution water oxidation may be one possible path for h+ harvesting. We discuss here the other possible paths and more particularly those leading to the physical and chemical degradation of the catalytic SCs. As the optical monitoring clearly shows that many SCs are indeed active in hydrogen evolution, restructuring processes and material damage were investigated, from the single SC to the single NP scale. It is first inspected by a correlative microscopy approach that couples optical microscopy with *post-mortem* scanning electron microscopy (SEM) in the same ROI, as exemplified in Figure 5a (other examples in Figure S4.1). Here, we chose a substrate region with larger SCs as they are likely to produce a larger amount of molecular hydrogen and therefore to cause more visible damage.

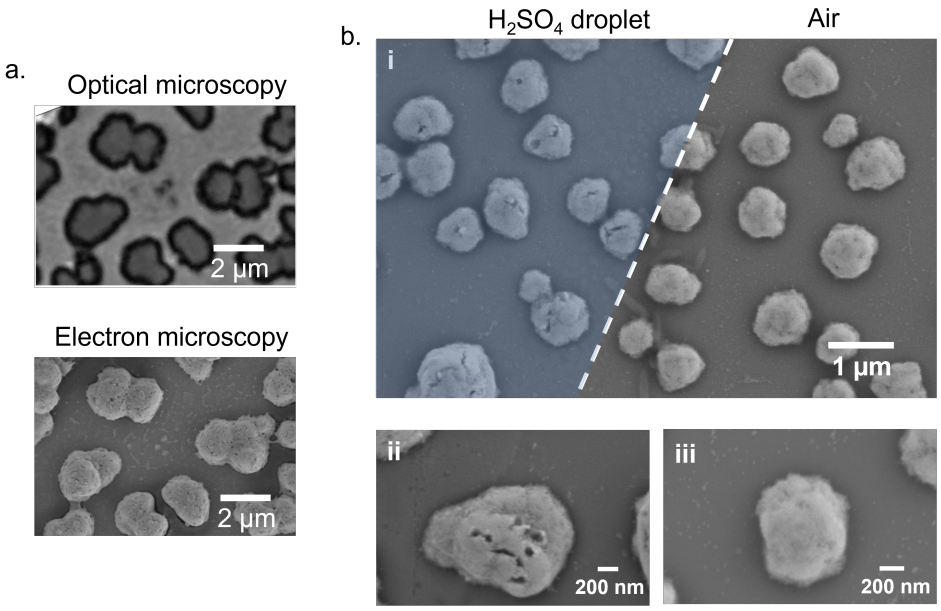

Figure 5. Correlative microscopy approach for visualizing the effects of the catalytic reaction at the single SC level. (a) Identical location optical and electron microscopy images of SCs immobilized on an ITO coverslip. (b) SEM image (i) recorded at the border (dashed line) of the droplet cell confining the photo-catalytic reaction and zoom over two single SCs inside (ii) and outside (iii) of the cell.

The most evident changes associated with the photocatalytic reaction are primarily observed in the microscale motion of the catalysts (SCs) on the substrate. This motion can be directly detected through optical image sequences. Figure S7.1 provides specific examples of SCs in motion on the ITO support. These images demonstrate that the production of gas induces movement in multiple SCs, as previously observed in the case of individual nanoscale electrocatalysts.[42] The motion of SCs implies that the mechanical forces, such as convection, resulting from hydrogen evolution, do not cause the complete disintegration of SCs into individual nanoparticles (NPs). Consequently, these forces are insufficient to break a significant number of attractive interactions between NPs.

Next, the effect of gas evolution can be seen within the single SC from same location SEM and optical images. Particularly, localizing the footprint of the droplet cell at the substrate surface in SEM images, as in Figure 5b, allows to compare, at high spatial resolution, the morphological changes induced by the gas evolution reaction at the single crystal level. In Figure 5b, the SCs located inside of the cell (Figure 5b ii) clearly show holes and cracks, while the crystals found outside remain unaffected (Figure 5b iii). We note that the size of the holes (ca. 100 nm) is compatible with the NB diameters found at the beginning of their growth, we believe this is evidence that H_2 evolution also leads to the erosion of the SC. The erosion of the crystal

suggests the existence of weak points in the crystal structure, which may be due to physical defects, such as stacking faults or grain boundaries. It may also arise from chemical weakening of the crystal, such as the corrosion induced by the HER reaction. Both causes would lead to the detachment of NPs from the SC and their release into solution. These structural rearrangements are likely to affect the crystal catalytic activity over time and could be at the origin of the intermittent activity evidenced in Figure 4.

SC and NP corrosion

Beyond mechanical erosion of the SCs, corrosion can also be associated with a chemical transformation of the SC and of its individual structural building block, the Ag@Pt NP. To apprehend the possible chemical corrosion of the SC or NP during HER, the reaction mechanism is first inspected in colloidal solution of Ag@Pt NPs. Colloidal Ag or Ag@Pt NPs solutions (containing 0.01 M metal precursor) in the presence of 0.05 M H_2SO_4 were irradiated by a polychromatic white light source and the optical properties of the colloidal dispersions were evaluated *in situ* by UV-Vis spectroscopy as reported in Figure 6a. While the plasmon characteristics of Ag NPs remain almost constant over 2 hours, the plasmon intensity of the Ag@Pt core-shell NPs rapidly decreases with time (linearly to a first approximation; decay rate of about 10 % per hour of irradiation). The Ag@Pt NPs' plasmon spectral changes are also associated, as mentioned above, with gas-bubble formation (see section SI8) attesting to the HER occurring under photo-activation. Moreover, this is also associated with an instantaneous and significant deposition of materials at the bottom of the spectroscopy cell upon addition of chloride ions (KCl). The deposit was further analysed by EDX spectroscopy and is found to be silver chloride salt, as shown in the EDX elemental spectrum of Figure S1.4.

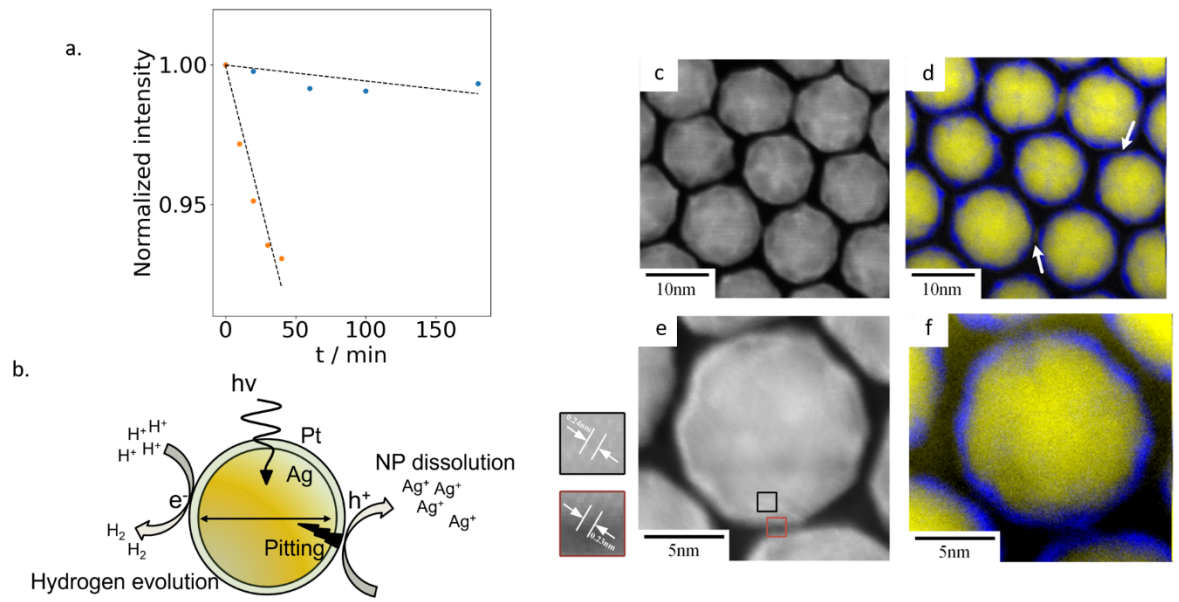

Figure 6. Unraveling the mechanism of plasmon assisted hydrogen production at the core-shell NP surface (a) Fluctuation of the maximum intensity of the plasmonic band as a function of irradiation time for 0.01 M of Ag NPs (blue dots) and Ag@Pt NPs dispersed in 0.01 M sulphuric acid solution (orange dots). (b) Scheme representing the redox process occurring at the NP surface. (c, e) High resolution STEM image of Ag@Pt NPs together with the corresponding EELS elemental mapping (d, f) highlighting the discontinuity of the Pt (blue) shell and the presence of silver (yellow) at the Pt outer surface.

The bulk experiment described above suggests the reductive HER step is accompanied by the oxidation of Ag into Ag^+. Indeed, when the NPs are irradiated by light, an e-/h+ pair is generated during the damping of the plasmonic excitation. The separation of this e-/h+ pair is then involved in an overall redox process schematized in Figure 6b. The excess of protons and presence of catalytic Pt atoms enables the fast consumption of the e- and H^+ into molecular H_2 through the HER (Equation 1). The counterpart anodic reaction (Equation 6) appears to be the oxidation of the less noble metal of the Ag@Pt NPs, i.e. the Ag atoms, by the h+. This corrosion of Ag from the NP core is at the origin of the progressive disappearance of the plasmonic band and, in the presence of Cl^- ions, to the concomitant precipitation of AgCl following Equation 7.

$$Ag + h^+ \rightarrow Ag^+ \quad (6)$$

$$Ag^+ + Cl^- \rightarrow AgCl_{(s)} \quad (7)$$

From a simplified theoretical model which considers an H_2/Ag ratio of 0.5 and a plasmonic intensity decay strictly linked to the symmetrical dissolution of the Ag core of the NPs, an H_2 production rate of 320 $nM.s^{-1}$ can be estimated for the colloidal solution of Ag@Pt NPs (details

in SI, section SI8). At the single NP level this would correspond to an average TOF of 2 H_2 mol.NP^{-1}.s^{-1}. This value can be compared to the HER activity of single SCs probed by optical microscopy in section 2.3.3, even though both experiments were not performed under the same light irradiance. If we consider an SC as a compact *fcc* 3D arrangement of NPs, one can evaluate a compactness constant of $p = \frac{\pi\sqrt{2}}{6} \approx 0.74$. For a 1 μm^3 SC and inter-NP separation distance of 3.6 nm, the number of NPs constituting the SC amounts to ~ 3.10^5. Based on the TOF for a single NP, the SC would be able to produce 6 10^5 mol.s^{-1}. This actually compares well to the 10^6 mol.s^{-1} TOF measured by the optical microscopy monitoring.

The mechanism described above then suggests that most of the Ag@Pt NPs of the catalytically active crystals (or at least at the crystal surface) would be available for oxidative corrosion. This may explain the mechanical erosion observed at the level of individual crystals, induced by a chemical degradation of individual NPs. The oxidative corrosion of the NPs may also affect the integrity of the NPs and of the SCs. For example in the absence of Cl^- ions one expects a dissolution of the core of the Ag@Pt NPs, while in the presence of Cl^- the Ag core would be converted into a less dense AgCl, yielding a size increase of the NP[43,44]). In the absence of Cl^- ions, H_2 evolution should be associated with dissolution of NPs from the SC. From the 10^6 H_2 mol.SC^{-1}.s^{-1}, a twice larger amount of Ag atoms dissolved would correspond the dissolution of ca. 36 NPs (assuming ca. 5.5 10^4 Ag atom per NP) within each SC. It is definitely small compared to the number of NP per SC and compared to the sizes of holes and cracks suggesting that the aforementioned erosion has both chemical (dissolution) and mechanical origins.

The origin of the chemical corrosion of the Ag@Pt NP requires atomic scale imaging of the individual NPs. The core-shell architecture and the integrity of the Pt layer were then analyzed by Scanning Transmission Electron Microscopy (STEM) in the High-Angle Annular Dark-Field (HAADF) mode, and using Electron Energy Loss Spectroscopy (EELS) for chemical mapping. Figures 6c and 6e show typical STEM-HAADF images of Ag@Pt NPs with Ag core and Pt shell in a dark and bright contrast respectively. This can be verified by the corresponding EELS maps (Figure 6d and 6f) with Ag core in yellow and Pt shell in blue.

The Ag@Pt NP surface seems rather homogeneous (Figure 6c-f). *A contrario*, the EELS mapping reveals discontinuities in the Pt shell and pitting that could indeed explain that the Ag core, not fully protected by the Pt layer, may corrode. The arrows in Figure 6d also highlight a very thin atomic layer of silver deposited on the Pt shell for a few NPs in a discontinuous manner. The outer Ag layer may be attributed to the possible competition of Pt ion reduction during the NP synthesis. The direct reduction of Pt ions by the oleylamine ligand at the Ag NP may compete with galvanic exchange of the Ag metal (producing Ag^+ ions and Pt metal deposit).

The dissolved Ag^+ may then be subsequently reduced by oleylamine during the synthesis step, which may lead to local deposition of Ag at the NP surface. The resulting structure is detrimental during the photocatalytic HER as it will promote access to the Ag NP core, thus accelerating the overall corrosion of the NP.

The low leakage of Ag^+ (proportional to the amount of hydrogen produced) should also result in a non-negligible layer of AgCl at the NP surface in presence of chloride ions that could be detrimental to the HER rate over time through a loss of efficiency of the light absorption and a poorer access to charge carriers in the Pt shell. Therefore, for practical applications, a more noble metal might be required. In addition, one should remember that for efficient HER a sacrificial reducer is required to consume the h^+, at least easier to oxidize than the plasmonic core of the NP.

3. Conclusion

Plasmonic SCs with *fcc* lattice and made of Ag@Pt core-shell NPs were successfully grown on solid support, as proved by TEM, SEM-EDX and GISAXS analyses. High resolution optical microscopy technique was then employed to evaluate quantitatively their photo-catalytic activity toward HER in acidic condition at the single SC level by detecting, counting and sizing *operando* single hydrogen NBs generated following light irradiation. Analyzing local optical intensity fluctuation also revealed three distinct SC behaviors: constant gas production, intermittent activity and total inactivity.

Degradation mechanisms were finally deciphered, in a top-down multi-imaging approach from the single SC level by correlative microscopy (same location optical and electron microscopy analysis) and then at the single NP level by high resolution STEM-HAADF coupled with EELS elemental mappings. Results show SCs are subjected to mechanical erosion during H_2 evolution suggesting the presence of weaker points in the SC structure. NPs also corrode in absence of h+ scavenger, after carriers' generation. Indeed, the excess of protons in solution and the presence of the Pt shell lead to the fast consumption of e- through HER. The counterpart anodic reaction is likely to be the oxidative dissolution of Ag core accessible because of the inhomogeneity of the Pt shell.

4. Experimental Section

Materials and chemicals

Chemicals were used as received without any further purification and stored under inert atmosphere. Sulphuric acid, silver nitrate, dioctyl ether, oleic acid (90%), chloroform (≥99%) and $Pt(acac)_2$ were purchased from Merck. Oleylamine (80-90%) was from ACROS Organics. Ultrapure water with a resistivity of 18.2 MΩ.cm was used to dilute the sulphuric acid.
ITO coverslips (Thickness #1.5) were purchased from SPI. The thickness of the conductive layer deposited on glass was 350 nm, corresponding to a resistivity of about 15-30 Ω.cm.
Pipettes were made by pulling borosilicate glass capillaries (outer and inner diameters of 1.0 mm and 0.5 mm, respectively) using a P-2000 laser puller from Sutter Instruments. The pipette tips were then polished using aluminum oxide tape (3 µm, from Precision Surfaces International) to obtain a final diameter < 50 µm before being filled with dilute sulphuric acid.

UV-Vis spectroscopy

Extinction spectra were recorded using a Varian Cary 5000 UV-Vis-NIR spectrometer. The NP concentration (C_{NPs}) was evaluated using the following equation:

$$C_{NPs} = \frac{C_M V_M}{\frac{4}{3}\pi\left(\frac{D_{core}}{2}\right)^3 Na}$$

where C_M is the total atomic concentration after synthesis, V_M the molar volume of metal, D the diameter of the NPs and Na the Avogadro number. C_M is determined using the Beer-Lambert Law.

Optical microscopy

Optical imaging was performed using a motorized inverted microscope (Zeiss, Axio Observer 7) equipped with a high numerical aperture objective (Zeiss Plan-Apochromat 63x/1.4 NA with oil immersion). The substrate was illuminated from the backside (glass side) with a white light source and the reflected light was collected by a CMOS camera (UI-3080CP Rev. 2, IDS) operating at 20 Hz.
The local photochemical experiments were conducted using an electrochemical Probe Scanner from Heka with a three-axis piezo stage that allows one to approach a pipette tip close to the surface and to create a chemical micro-droplet cell. The whole setup was mounted on an isolation table that actively reduces the mechanical noise.

Electron microscopy and cross-correlation

SEM-EDX and correlative microscopy approach

SEM analyses on ITO substrates were performed on a Gemini SEM 360 from Zeiss equipped with an energy dispersive X-ray detector from Oxford Instruments. For elemental analyses, the microscope aperture size was expanded to 60 µm. The data were processed using the Aztec software.
Correlative microscopy analyses (same location in optical and electron microscopy) were achieved using a specific marked substrate holder from Zeiss allowing retrieval of the same position in optical and electron microscopies for imaging. The data were processed using the Zeiss ZEN Blue software and the ZEN Connect module.

TEM

TEM images were recorded with a JEOL JEM1011 electron microscope with an acceleration voltage of 100 kV. Prior to the visualization, NPs were drop-casted from a diluted solution onto a carbon-coated copper grid. For observing crystals, NPs were deposited using anti-capillary tweezers.

STEM-EELS

Scanning TEM (STEM) images were acquired using a high-angle annular dark-field (HAADF) detector in a Nion Ultrastem 200 Cs-corrected microscope operating at 100kV with a probe size of about 0.07 nm. The probe convergence and HAADF detector minimum collection semi-angles were 35 and 75 mrad respectively, meaning that HAADF images were dominated by Z-contrast, although some diffraction contrast is possible. Elemental maps were obtained using electron energy-loss spectroscopy (EELS) in the spectrum-image (SI) collection mode using the Ag M- and Pt M-edges.

GISAXS

GISAXS was performed in Orsay with a rotating copper anode generator operated at 40 kV and 20 mA (small focus: 0.1 Å~ 0.1 mm^2 in cross section). The optics consist of two parabolic

multilayer graded mirrors in K−B geometry, which deliver a well-defined and intense parallel monochromatic beam. Photostimulable imaging plates are used as detector. The reading of the exposed imaging plate is performed by a STORM 820 scanner (Molecular Dynamics).

Supporting Information

Supporting Information is available from the Wiley Online Library or from the author.

Acknowledgements

This work was partially financially supported by the Agence Nationale de la Recherche (ANR) Jeunes chercheuses, jeunes chercheurs, ANR JCJC, program (PIRaNa project, ANR-20-CE42-000) and through the CNRS and Université Paris Cité. JMN, FK and JFL acknowledge the ITODYS SEM facility, the Ile-de-France region and IDEX for financial support of the AFMBeam-Rex platform. AC and CS thank the Chinese Scholarship Council for the thesis grant of YF. They thank also Sorbonne University and the CNRS for their facilities, and finally acknowledge Dr. P-A. Albouy for the GISAXS experiments in the LPS laboratory.

Received: ((will be filled in by the editorial staff))
Revised: ((will be filled in by the editorial staff))
Published online: ((will be filled in by the editorial staff))

References

[1] M. Lou, J. L. Bao, L. Zhou, G. N. Naidu, H. Robatjazi, A. I. Bayles, H. O. Everitt, P. Nordlander, E. A. Carter, N. J. Halas, *ACS Energy Lett.* **2022**, *7*, 3666.

[2] D. Devasia, A. J. Wilson, J. Heo, V. Mohan, P. K. Jain, *Nat. Commun.* **2021**, *12*, 2612.

[3] K. A. Willets, R. P. Van Duyne, *Annu. Rev. Phys. Chem.* **2007**, *58*, 267.

[4] G. Baffou, R. Quidant, *Chem. Soc. Rev.* **2014**, *43*, 3898.

[5] S. Yu, P. K. Jain, *Angew. Chemie - Int. Ed.* **2020**, *59*, 2085.

[6] L. Zhou, D. F. Swearer, C. Zhang, H. Robatjazi, H. Zhao, L. Henderson, L. Dong, P. Christopher, E. A. Carter, P. Nordlander, N. J. Halas, *Science* **2018**, *362*, 69.

[7] D. Devasia, A. Das, V. Mohan, P. K. Jain, *Annu. Rev. Phys. Chem.* **2021**, *72*, 423.

[8] A. Marimuthu, J. Zhang, S. Linic, *Science* **2013**, *340*, 1590.

[9] H.-J. Wang, J.-S. Lin, H. Zhang, Y.-J. Zhang, J.-F. Li, *Accounts Mater. Res.* **2022**, *3*, 187.

[10] Y. Chen, Y. Zhai, L. Deng, N. Wang, Y. Mao, J. Yang, Y. Huang, *Appl. Phys. Lett.* **2019**, *114*, 183902.

[11] J.-F. Lemineur, S. Schuermans, J. Marae-Djouda, T. Maurer, A. M. Ritcey, *J. Phys. Chem. C* **2016**, *120*, 8883.

[12] D. García-Lojo, S. Núñez-Sánchez, S. Gómez-Graña, M. Grzelczak, I. Pastoriza-Santos, J. Pérez-Juste, L. M. Liz-Marzán, *Acc. Chem. Res.* **2019**, *52*, 1855.

[13] M. Blanco-Formoso, N. Pazos-Perez, R. A. Alvarez-Puebla, *ACS Omega* **2020**, *5*, 25485.

[14] I. Coropceanu, E. M. Janke, J. Portner, D. Haubold, T. D. Nguyen, A. Das, C. P. N. Tanner, J. K. Utterback, S. W. Teitelbaum, M. H. Hudson, N. A. Sarma, A. M. Hinkle, C. J. Tassone, A. Eychmüller, D. T. Limmer, M. O. de la Cruz, N. S. Ginsberg, D. V. Talapin, *Science* **2022**, *375*, 1422.

[15] J. Lyu, W. Chaâbani, E. Modin, A. Chuvilin, T. Bizien, F. Smallenburg, M. Impéror-Clerc, D. Constantin, C. Hamon, *Adv. Mater.* **2022**, *34*, 2200883.

[16] L. Chapus, P. Aubertin, S. Joiret, I. T. Lucas, E. Maisonhaute, A. Courty, *ChemPhysChem* **2017**, *18*, 3066.

[17] N. Cheng, S. Stambula, D. Wang, M. N. Banis, J. Liu, A. Riese, B. Xiao, R. Li, T. K. Sham, L. M. Liu, G. A. Botton, X. Sun, *Nat. Commun.* **2016**, *7*, 13638.

[18] J.-F. Lemineur, H. Wang, W. Wang, F. Kanoufi, *Annu. Rev. Anal. Chem.* **2022**, *15*, 57.

[19] J. F. Lemineur, P. Ciocci, J.-M. Noël, H. Ge, C. Combellas, F. Kanoufi, *ACS Nano* **2021**, *15*, 2643.

[20] P. Ciocci, J. F. Lemineur, J.-M. Noël, C. Combellas, F. Kanoufi, *Electrochim. Acta* **2021**, *386*, 138498.

[21] S. Xu, X. Yu, Z. Chen, Y. Zeng, L. Guo, L. Li, F. Luo, J. Wang, B. Qiu, Z. Lin, *Anal. Chem.* **2020**, *92*, 9016.

[22] S. Li, Y. Du, T. He, Y. Shen, C. Bai, F. Ning, X. Hu, W. Wang, S. Xi, X. Zhou, *J. Am. Chem. Soc.* **2017**, *139*, 14277.

[23] T. Zhang, S. Li, Y. Du, T. He, Y. Shen, C. Bai, Y. Huang, X. Zhou, *J. Phys. Chem. Lett.* **2018**, *9*, 5630.

[24] Y. Fang, Z. Li, Y. Jiang, X. Wang, H.-Y. Chen, N. Tao, W. Wang, *Proc. Natl. Acad. Sci.* **2017**, *114*, 10566.

[25] L. Godeffroy, J.-F. Lemineur, V. Shkirskiy, M. Miranda Vieira, J.-M. Noël, F. Kanoufi, *Small Methods* **2022**, *6*, 2200659.

[26] Y. Fan, A. Girard, M. Waals, C. Salzemann, A. Courty, *ACS Appl. Nano Mater.* **2023**, *6*, 1193.

[27] S. Lee, A. T. Ngo, I. Lisiecki, A. Courty, *Mater. Chem. Front.* **2022**, *6*, 1814.

[28] K. Reilly, B. Fang, F. Taghipour, D. P. Wilkinson, *J. Catal.* **2017**, *353*, 63.

[29] A. Courty, J. Richardi, P. A. Albouy, M.-P. Pileni, *Chem. Mater.* **2011**, *23*, 4186.

[30] K. Ouhenia-Ouadahi, A. Andrieux-Ledier, J. Richardi, P. A. Albouy, P. Beaunier, P. Sutter, E. Sutter, A. Courty, *Chem. Mater.* **2016**, *28*, 4380.

[31] R. W. Taylor, V. Sandoghdar, *Nano Lett.* **2019**, *19*, 4827.

[32] M. Mahamdeh, S. Simmert, A. Luchniak, E. Schäffer, J. Howard, *J. Microsc.* **2018**, *272*, 60.

[33] A. J. Merryweather, Q. Jacquet, S. P. Emge, C. Schnedermann, A. Rao, C. P. Grey, *Nat. Mater.* **2022**, *21*, 1306.

[34] A. J. Merryweather, C. Schnedermann, Q. Jacquet, C. P. Grey, A. Rao, *Nature* **2021**, *594*, 522.

[35] C. Xu, A. J. Merryweather, S. S. Pandurangi, Z. Lun, D. S. Hall, V. S. Deshpande, N. A. Fleck, C. Schnedermann, A. Rao, C. P. Grey, *Joule* **2022**, *6*, 2535.

[36] C. L. Bentley, J. Edmondson, G. N. Meloni, D. Perry, V. Shkirskiy, P. R. Unwin, *Anal. Chem.* **2019**, *91*, 84.

[37] X. Xu, D. Valavanis, P. Ciocci, S. Confederat, F. Marcuccio, J. Lemineur, P. Actis, F. Kanoufi, P. R. Unwin, *Anal. Chem.* **2023**, *95*, 319.

[38] E. B. Tetteh, D. Valavanis, E. Daviddi, X. Xu, C. S. Santos, E. Ventosa, D. Martín-yerga, W. Schuhmann, P. R. Unwin, *Angew. Chemie - Int. Ed.* **2023**, *62*, e202214493.

[39] P. Saha, J. W. Hill, J. D. Walmsley, C. M. Hill, *Anal. Chem.* **2018**, *90*, 12832.

[40] H. M. Dastjerdi, M. Dahmardeh, A. Gemeinhardt, R. G. Mahmoodabadi, H. Köstler, V. Sandoghdar, *J. Phys. D. Appl. Phys.* **2022**, *55*, 054002.

[41] J. Ustarroz, I. M. Ornelas, G. Zhang, D. Perry, M. Kang, C. L. Bentley, M. Walker, P. R. Unwin, *ACS Catal.* **2018**, *8*, 6775.

[42] J. Wang, L. Zhang, J. Xie, Y. Weizmann, D. Li, J. Li, *Nano Lett.* **2022**, *22*, 5495.

[43] J. G. Smith, X. Zhang, P. K. Jain, *J. Mater. Chem. A* **2017**, *5*, 11940.

[44] M.-C. Nguyen, P. Berto, F. Valentino, J.-F. Lemineur, J.-M. Noel, F. Kanoufi, G. Tessier, *ACS Nano* **2022**, *16*, 14422.

The photo-catalytic activity of plasmonic supercrystals made of Ag@Pt NPs is monitored through *operando* nanobubbles imaging by high-resolution optical microscopy. The degradation mechanisms following light irradiation is investigated at the single supercrystal and nanoparticle level by correlative microscopy and high resolution STEM-EELS, respectively.

Y. Fan,[1] M. Walls,[2] C. Salzemann,[1] J.-M. Noël,[3] F. Kanoufi,[3] A. Courty, [1] J.-F. Lemineur[3]**

Metal Core-Shell Nanoparticle Supercrystals: from Photo-Activation of Hydrogen Evolution to Photo-Corrosion

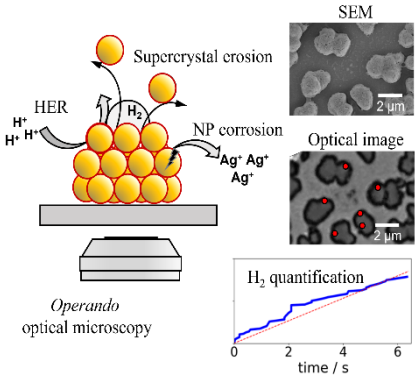

Supporting Information

Metal Core-Shell Nanoparticle Supercrystals: from Photo-Activation of Hydrogen Evolution to Photo-Corrosion

Yinan Fan,[1] Michael Walls,[2] Caroline Salzemann,[1] Jean-Marc Noël,[3] Frédéric Kanoufi,[3] Alexa. Courty, [1] Jean-François Lemineur[3]**

Table of contents

SI1. Bulk experiments

SI2. EDX analyses on SCs

SI3. GISAXS

SI4. Example of co-localization

SI5. Optical tracking of NB nucleation

SI6. Relationship between NB size and optical intensity

SI7. SC motion upon bubble nucleation

SI8. Mie calculation

SI1. Bulk experiments

UV-Vis spectroscopy experiments were performed in bulk with a colloidal solution of (Ag, Pt or Ag@Pt) NPs dispersed in 50 mM of H_2SO_4 under white light irradiation. At the end of the UV-Vis monitoring, potassium chloride was added to precipitate the possible ions. The results are resumed below.

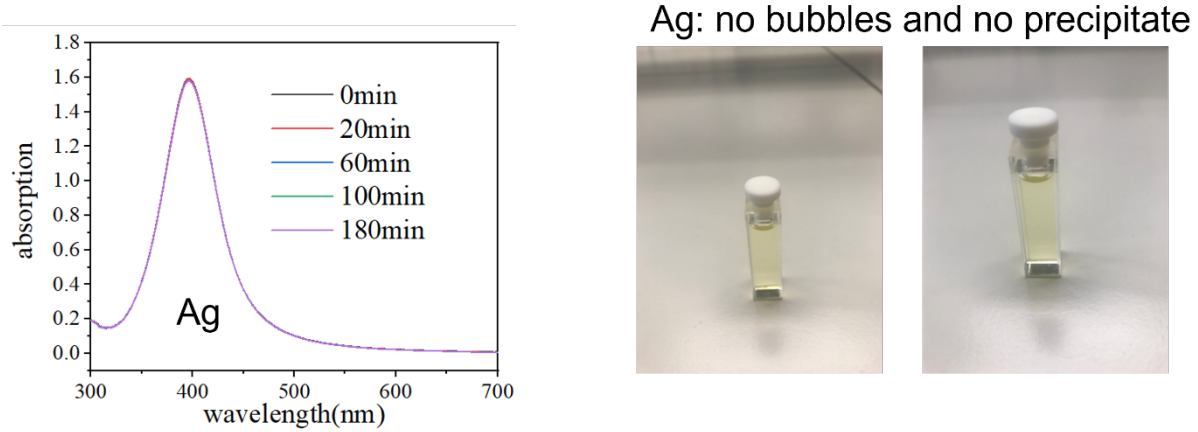

Figure S1.1. UV-Vis spectroscopy of Ag NPs dispersed in 50 mM of sulfuric acid as a function of time and under light irradiation. The image of the spectroscopy cell shows that no bubbles are formed after 180 min of irradiation. No precipitate is observed after the addition of KCl into the cell.

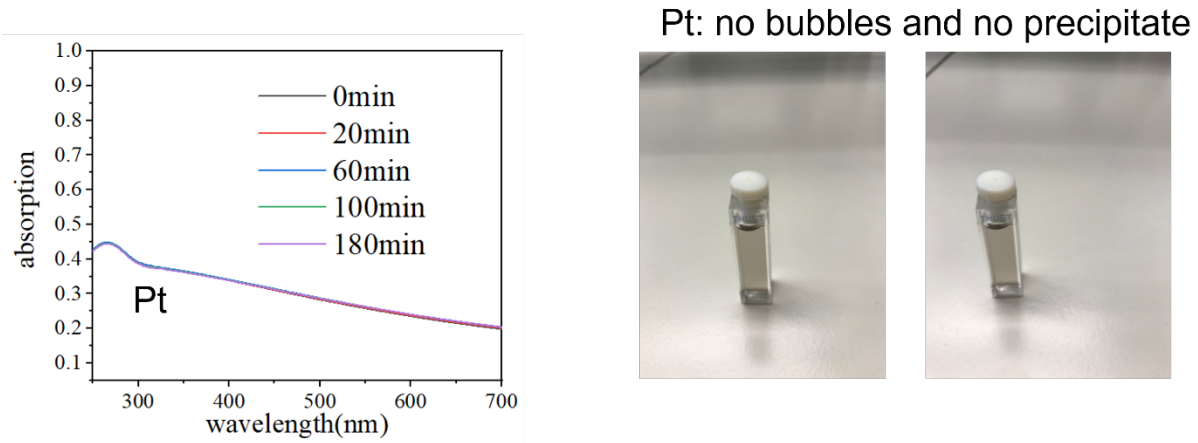

Figure S1.2. UV-Vis spectroscopy of Pt NPs dispersed in 50 mM of sulfuric acid as a function of time and under light irradiation. The image of the spectroscopy cell shows that no bubbles are formed after 180 min of irradiation. No precipitate is observed after the addition of KCl into the cell.

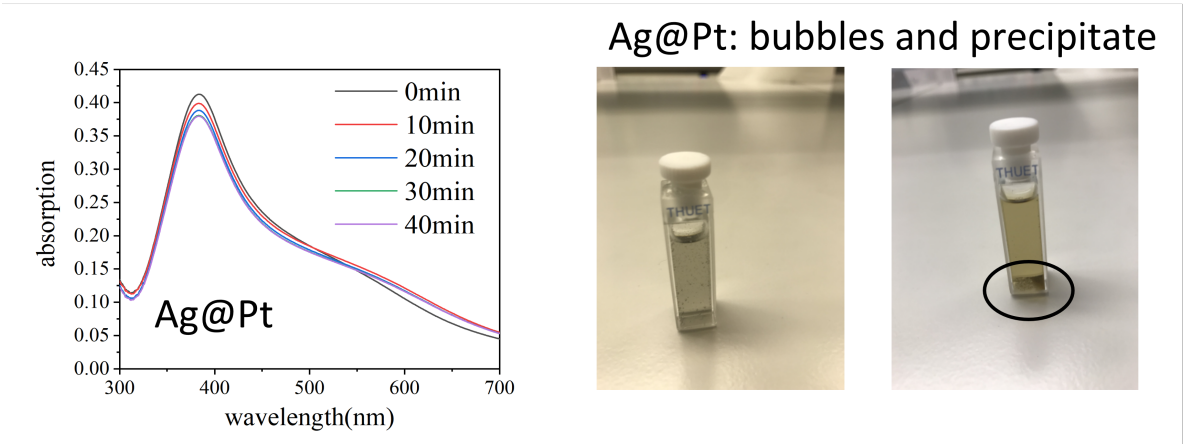

Figure S1.3. UV-Vis spectroscopy of Ag@Pt NPs dispersed in 50 mM of sulfuric acid as a function of time and under light irradiation. The image of the spectroscopy cell shows bubbles appearing after few minutes of irradiation. In addition, a precipitate is detected after the addition of KCl. The black circle in the right image highlights the presence of the precipitate.

The precipitate was further collected and analysed by EDX spectroscopy and was identified as silver chloride.

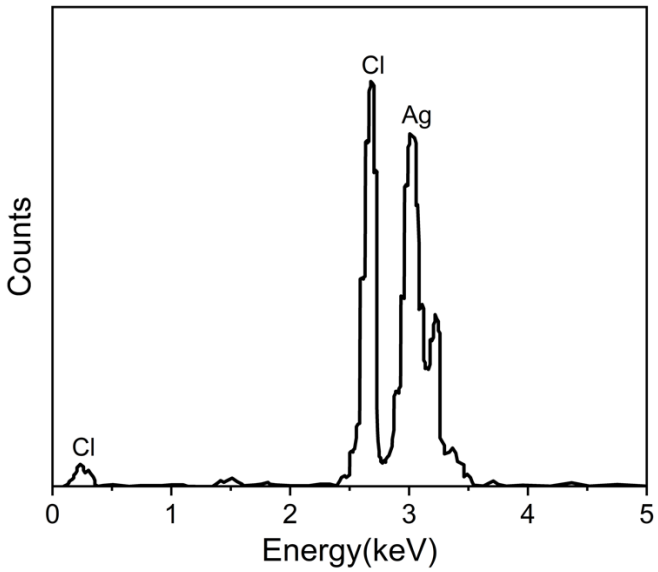

Figure S1.4. EDX spectrum of the precipitate collected after irradiating Ag@Pt NPs for 50 minutes and after adding KCl into the NP dispersion.

SI2. EDX analyses on SCs

Several EDX mapping have been recorded on 3 dimensional SCs and disorganized Ag@Pt NP array. The SCs have the same atomic composition as the NPs. The chemical analyses also show a perfectly homogeneous repartition of Ag and Pt atoms inside the SCs. In addition, the atomic composition of Ag@Pt NPs deduced from EDX analysis agrees with the one calculated from TEM images. The EDX analyses are resumed in Table S2.1 below.

EDS composition for NPs		**EDX composition for SCs**	
% Ag	% Pt	% Ag	% Pt
83	17	82	18

Table S2.1. Atomic composition obtained through EDX analysis for Ag@Pt NP arrays and SCs.

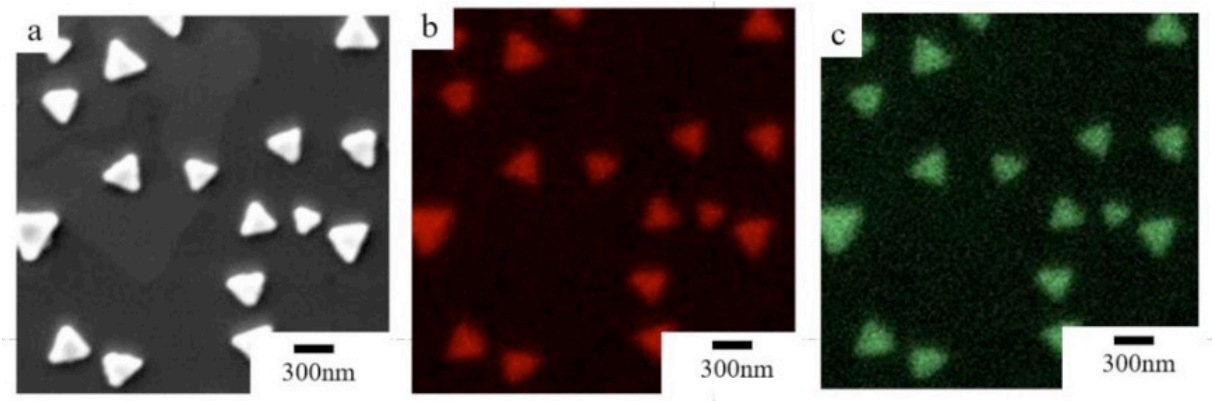

Figure S2.1. SEM image (a) and EDX mapping (b and c) of a second deposit obtained by drop-casting 20 µl of Ag@Pt NPs (0.01 M in toluene) at the surface of an ITO substrate. (b) and (c) correspond to Ag and Pt respectively.

SI3. GISAXS

From the positions of the Bragg reflections, the core-to-core interparticle distance Dc-c between Ag@Pt NPs can be estimated in the case of *fcc* arrangement, from the d(111) spacing by Dc–c = d(111)×√(3⁄2). The line profiles along 2θ (Figure S3.1.b) give a stacking periodicity of d(111)~13.9 nm, corresponding to Dc-c~17.0nm. Thus the average inter-particle distance (deduced from Dc-c-2R, R being the radius of the Ag@Pt NPs) is 3.6 ± 0.4 nm in agreement with a long OLA chain (2.04 nm) and a low interdigitation.

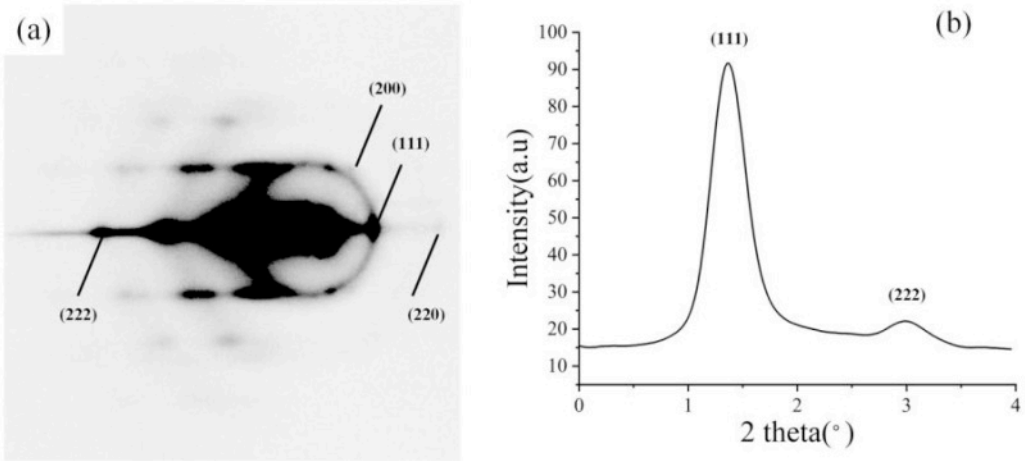

Figure SI3.1. GISAXS patterns of (a) Ag@Pt SCs and (b) intensity vs 2θ plotted from (a). The C=C double bond in the middle of the chain of OLA is a particular feature of this molecule which supposes during the organization of the nanoparticles a partial interdigitation as schematized in Figure SI3.2, in agreement with the results of Borges *et al.*[1]

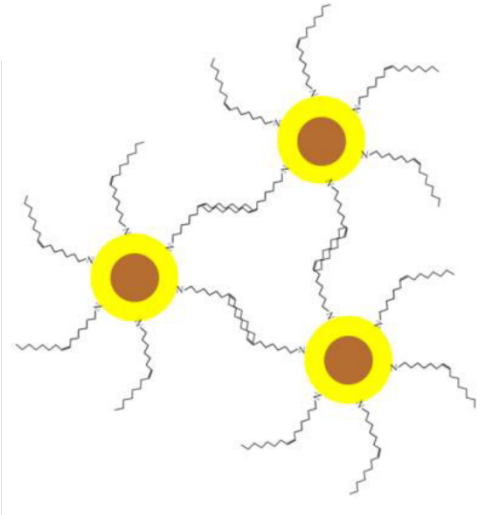

Figure SI3.2. Diagram of the molecular interdigitation of OLA ligands at the NP surface in a triangular organization

SI4. Example of co-localization

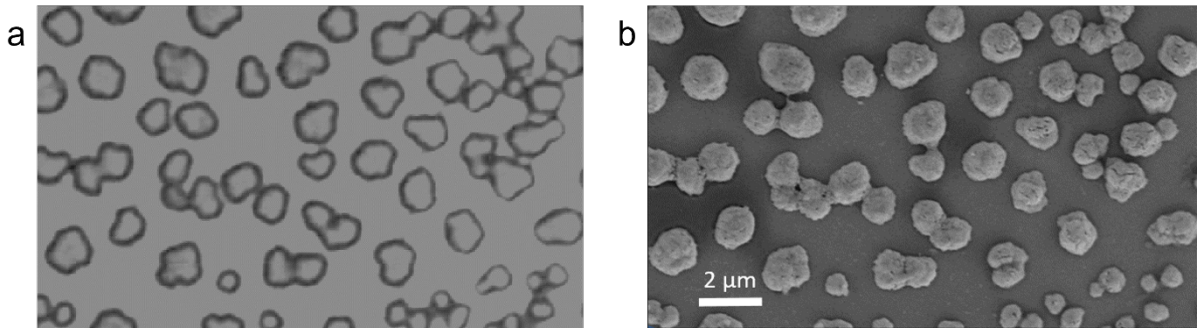

Figure SI4.1. Images of the same SCs recorded by (a) optical and (b) scanning electron microscopy.

SI5. Optical tracking of NB nucleation

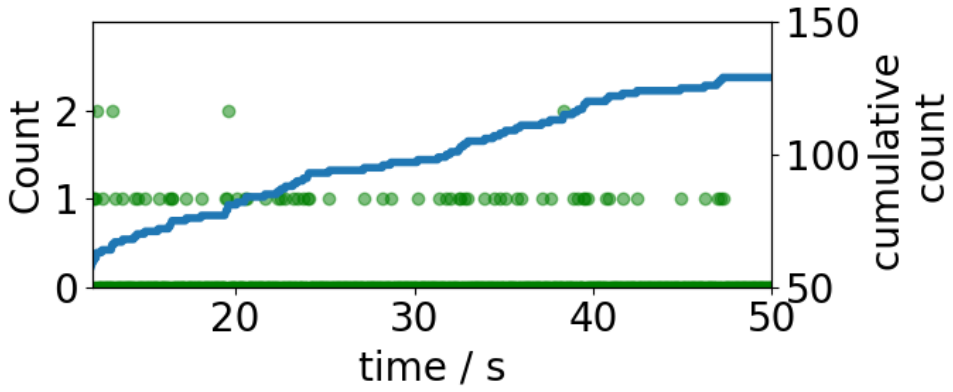

Figure SI5.1. Automatic NB counting in the same substrate region as presented in Figure 3 but over a longer period of time. Green dots correspond to nucleation events and the blue curve is the cumulative count. The rate of NB production still appears to be constant.

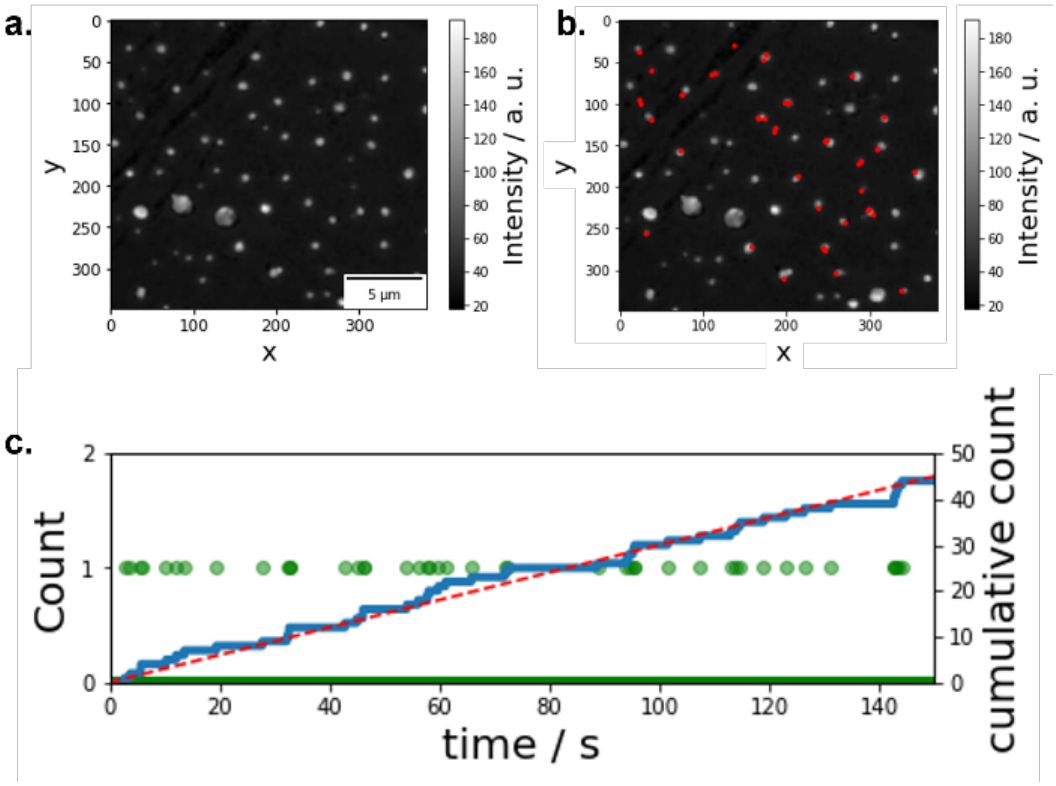

Figure SI5.2. Automatic NB counting in a second substrate area but for the same deposit as presented in Figure 3. Optical image (a) of the SCs and (b) optical mapping of NB nucleation events during 150 s. It takes > 20 times longer to reach the same gas production than in the area presented in Figure 3.

SI6. Relationship between NB size and optical intensity

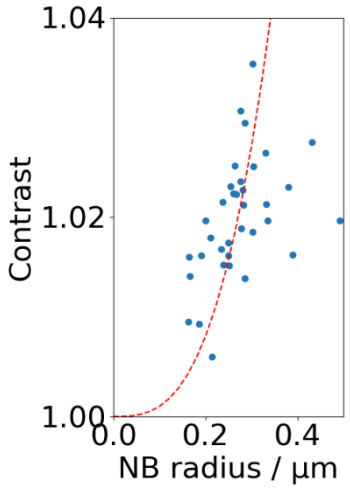

Figure SI6.1. Relationship between the optical intensity and the NB diameter which is further used to calculate the distribution of turn-over frequency at single crystals. The optical contrast is proportional to the NB volume (NB radius to the power of 3) which agrees well with the theory related to interferometric microscopy described in reference 2.

SI7. SC motion upon bubble nucleation

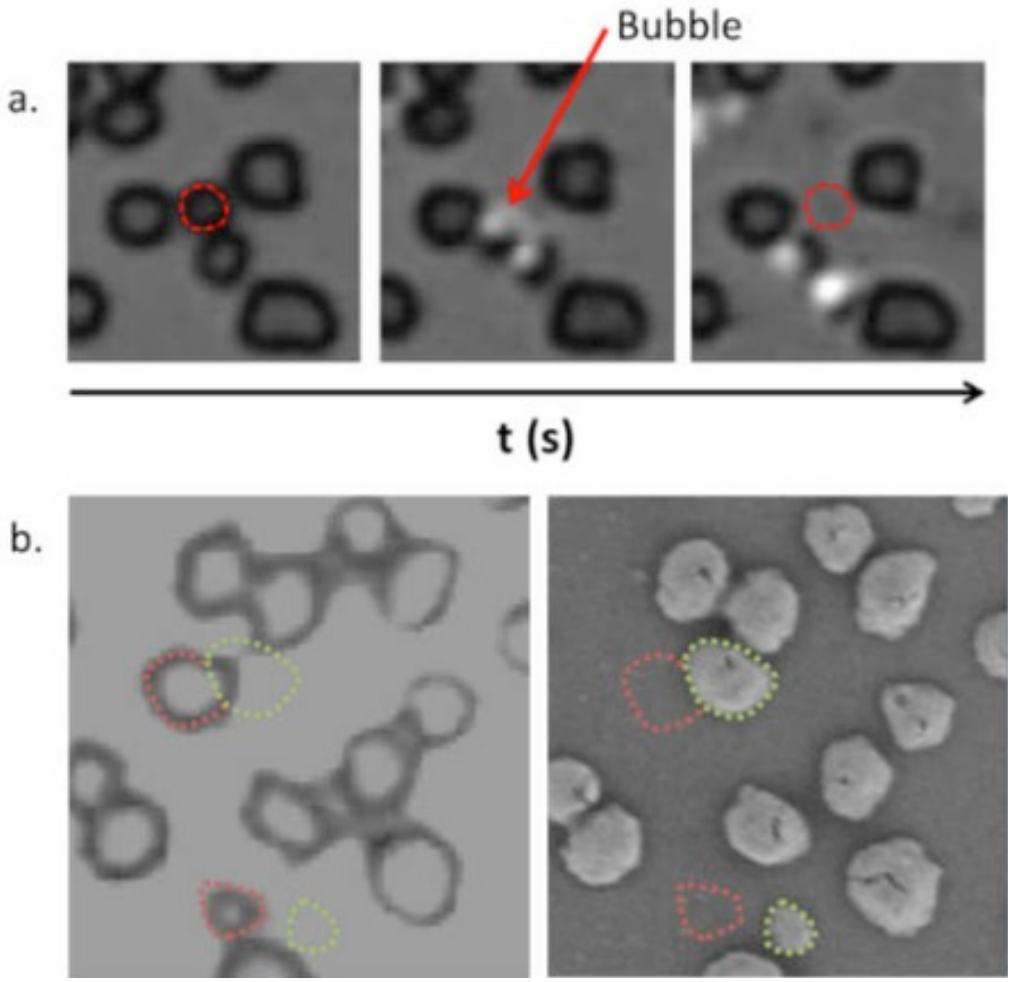

Figure SI7.1. Image sequence (a) recorded by optical microscopy that shows the motion of an entire SC caused by the growth of a hydrogen bubble highlighted by the red arrow. Correlative microscopy results (b; optical microscopy and SEM on the left and right, respectively) proving that two SCs have moved. Optical microscopy image has been recorded at the beginning of the photoactivation while SEM image is post-mortem.

SI8. Mie simulation

Extinction spectra were calculated using the Mie theory and a variable core-shell geometry in which the Pt shell thickness remains constant and the Ag core size is gradually reduced to mimic the (symmetrical) dissolution of Ag. According to calculations, the plasmonic band decreases linearly with the shrinking of the Ag core size when the Pt shell thickness is kept constant. As the dissolution of the Ag core is proportional to the production of molecular hydrogen (through the redox process related to both the consumption of e- and h+), one can estimated from the decay of the plasmonic band intensity a quantity of produced H_2 molecules.

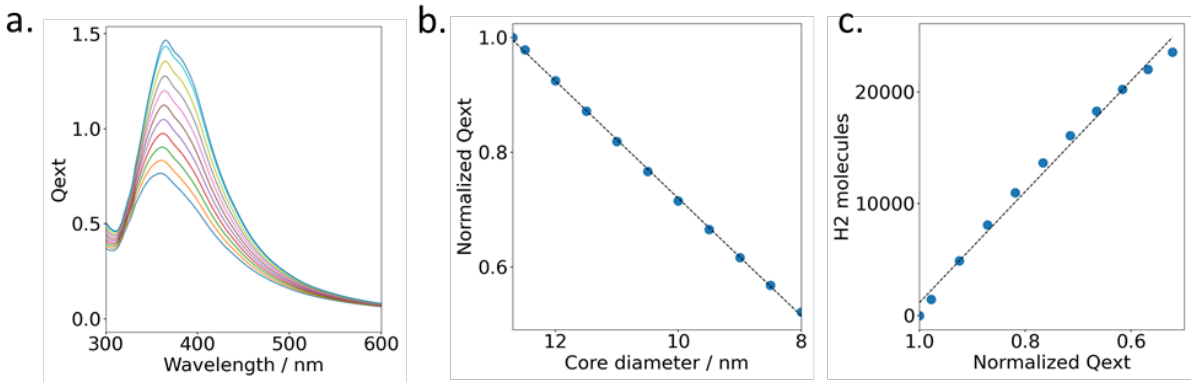

Figure SI8.1. Extinction spectra (a) calculated using the Mie theory with a variable core-shell geometry (Pt shell thickness constant and core size gradually reduced). Palik's optical constants have been used as well as a surrounding medium refractive index of 1.33. Plot (b) showing the apparent linear relationship between the plasmon band maximum intensity and the Ag core size for a model core-shell Ag@Pt NP structure. Production of molecular hydrogen as function of the weakening of the plasmon band intensity.

SI9. References

1. J. Borges, J. A. Ribeiro, E. M. Pereira, C. A. Carreira, C. M. Pereira, F. Silva. Preparation and characterization of DNA films using oleylamine modified Au surfaces. *J. Colloid Interface Sci.* **2011**, 458, 626-634.
2. R. W. Taylor and V. Sandoghdar. Interferometric Scattering Microscopy: Seeing Single Nanoparticles and Molecules via Rayleigh Scattering. *Nano Lett.* **2019**, 19, 4827-4835.